

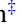


## Order parameters for antiferromagnetic structures: A first-principles study of iridium manganese

Flynn Walsh <sup>\*</sup>, Anirudh Raju Natarajan <sup>†</sup>, and Anton Van der Ven <sup>‡</sup>  
Materials Department, University of California, Santa Barbara, California 93106, USA

 (Received 21 November 2021; accepted 1 March 2022; published 4 April 2022)

We use density-functional theory to study the ordered states of iridium manganese, demonstrating a simple but powerful method for describing magnetic structures and the transitions among them. As an illustrative example, the coupling of magnetism and crystal structure in IrMn is examined through a rigorous exploration of strain space. We then generate order parameters for the ground-state magnetic structures, providing a comprehensive framework for understanding antiferromagnetic variants and their magnetic anisotropy. In particular, we show how the most direct path between two variant structures can be analytically determined; this technique is used to equate two seemingly contradictory prior studies.

DOI: [10.1103/PhysRevMaterials.6.044402](https://doi.org/10.1103/PhysRevMaterials.6.044402)

## I. INTRODUCTION

The net-zero, ordered local moments of antiferromagnets are both scientifically interesting and technologically exciting. Traditionally used to exchange bias ferromagnetic (FM) layers in thin films [1], antiferromagnetic (AFM) components are increasingly performing active roles in spintronic devices for qualities including significantly faster domain switching and the absence of stray magnetic fields [2,3]. Many of these applications are fundamentally concerned with the boundaries, or walls, of AFM domains, the orientationally distinct but symmetrically equivalent arrangements of moments that independently nucleate within a single grain below a crystal's Néel temperature. The magnetic anisotropy of a material—the energetics of the collective orientation of its moments—is of particular interest, although the anisotropy of noncollinear AFM structures is somewhat more complicated than that of FM materials, in which all spins align along a single axis.

The iridium manganese system has received significant attention for this reason, with notable anisotropy attributable to large Mn moments interacting with the  $5d$  orbitals of non-magnetic Ir. Equiatomic IrMn adopts an  $L1_0$  structure, which can be understood as a nearly fcc lattice containing alternate layers of Ir and Mn in a slightly compressed [001] direction. The Mn layers favor an in-plane checkerboard AFM ordering. The system's other ordered compound is  $L1_2$  IrMn<sub>3</sub>, in which Ir and Mn atoms, respectively, occupy the corners and faces of the conventional fcc unit cell [4,5]; Mn sites form kagomé lattices in {111} planes, leading to a noncollinear simple triangular magnetic structure [5,6]. This compound is of particular interest for its ability to exchange bias thin-film heterostructures and spin-valve devices [7–9]. It additionally exhibits remarkable Hall conductivity under the application

of spin-orbit torque [10,11] and is predicted to display the anomalous Hall effect [12]. Largely amorphous thin films of high Mn compositions are also commonly used in experiments, however those are presumably metastable and rarely well characterized [13]. Okamoto [4] additionally notes the potential existence of an unquenchable B2  $\beta$ -IrMn phase at temperatures above 1213 K, very close to its experimentally observed Néel temperature of approximately 1150 K [4].

The collinear magnetic anisotropy of IrMn is relatively well understood, but theoretical predictions of giant magnetic anisotropy energy (MAE) in IrMn<sub>3</sub>, obtained by rotating all moments around a common direction [14–16], are much larger than values measured in chemically disordered samples [17,18]. While Szunyogh *et al.* [16] believed that the discrepancy originates from the condition of experimental material, Jenkins *et al.* [19] recently argued that large MAE is not realized on account of the existence of lower-energy paths connecting magnetic domains. We find that the calculations of these two studies are basically equivalent and that the apparent disagreement is primarily one of semantics and experimental interpretation. This example—and the general lack of rigorous methods for studying AFM anisotropy—motivates a more complete approach to exploring the configuration space of AFM structures.

Specifically, we seek a framework for describing ordered arrangements of moments that is more concise than simply defining  $\mathbf{m}_i = (m_i^x, m_i^y, m_i^z)$  at every atomic site  $i$  in a tiling unit cell. Experimental literature commonly uses ad hoc order parameters (OPs) such as net moment, spin chirality, and sublattice magnetization to express experimental results (e.g., [10,20,21]), but these are typically motivated by interest in specific quantities rather than a comprehensive description of structures. Several general, group-theoretically motivated frameworks for OP generation also exist [22–25]. Because AFM order is typically associated with one irreducible representation of a crystal's space group (by Landau's theory of phase transitions), that irreducible representation's basis functions make natural order parameters for describing and identifying atomic structures, as often used in scattering experiments [26,27]. However, this approach requires the use of tabulated databases, in which basis functions are typically expressed for optimally describing phase transitions rather

<sup>\*</sup>Present address: Materials Sciences Division, Lawrence Berkeley National Laboratory, Berkeley, CA 94720, USA.

<sup>†</sup>Present address: Laboratory of Materials Design and Simulation, IMX, École Polytechnique Fédérale de Lausanne, 1015 Lausanne, Switzerland.

<sup>‡</sup>avdv@ucsb.edu

than distinguishing among symmetrically equivalent structures, as is essential for studying domain walls and magnetic anisotropy.

Drawing from several of these approaches, Sec. II outlines a simple procedure for determining useful OPs for AFM structures and the pathways among them, in principle similar to the theory applied to scalar occupational order in Ref. [25]. Providing a didactic example, we first use strain OPs to describe the deformation of IrMn, offering a comparison of magnetic states in Sec. IV A. These results reveal how the compound's stability is closely linked to its magnetic structure, and they highlight the remarkable energy reduction associated with IrMn's optimal AFM ordering. Sections IV B and IV C then generate OPs for the AFM ground states of IrMn and IrMn<sub>3</sub>, which are used to study magnetic anisotropy and the energies of magnetic structures representing domain walls in a manner applicable to a wide range of AFM materials.

## II. ORDER PARAMETERS

### A. A simple example

Order parameters (OPs) are used to concisely describe portions of a higher-dimensional space, which can be denoted generally as  $\sigma$ . While we are ultimately interested in representing magnetic structure, a simpler example is the three-dimensional space of normal strain. Assuming no shear,  $\sigma^T = (\epsilon_{xx}, \epsilon_{yy}, \epsilon_{zz})$  measures the strain of a crystal relative to a high-symmetry reference state. Every vector in  $\sigma$  describes a specific crystal deformation, for instance a Bain transformation that tetragonally distorts a bcc lattice to an fcc one.

For a conventional bcc unit cell under Hencky (true) strain, one such Bain transformation is the vector

$$\mathbf{v}_1^T = \frac{\ln 2}{6}(-1, -1, 2), \quad (1)$$

which corresponds to elongation along the  $z$ -axis and volume-conserving compression in  $x$  and  $y$ . Due to the cubic symmetry of the bcc reference state, symmetrically equivalent fcc structures can be found at

$$\mathbf{v}_2^T = \frac{\ln 2}{6}(-1, 2, -1) \quad (2)$$

and

$$\mathbf{v}_3^T = \frac{\ln 2}{6}(2, -1, -1). \quad (3)$$

Figure 1 plots these three fcc variants within the space of  $\sigma$ . As illustrated, the variants lie in a two-dimensional plane that (under Hencky strain) includes the bcc reference state. The Bain paths can therefore be described using only two parameters, which are conventionally chosen as [23]

$$\eta_2 = (\epsilon_{xx} - \epsilon_{yy})/\sqrt{2}, \quad (4)$$

$$\eta_3 = (2\epsilon_{zz} - \epsilon_{xx} - \epsilon_{yy})/\sqrt{6}. \quad (5)$$

In Fig. 1,  $\eta_2$  and  $\eta_3$  are drawn as a new pair of axes. This subspace possesses an important symmetry with respect to the point group of the reference bcc structure; vectors in the  $\eta_2$ - $\eta_3$  plane may only be rotated in-plane by the application of any point group operation of bcc. The space spanned by  $\eta_2$  and

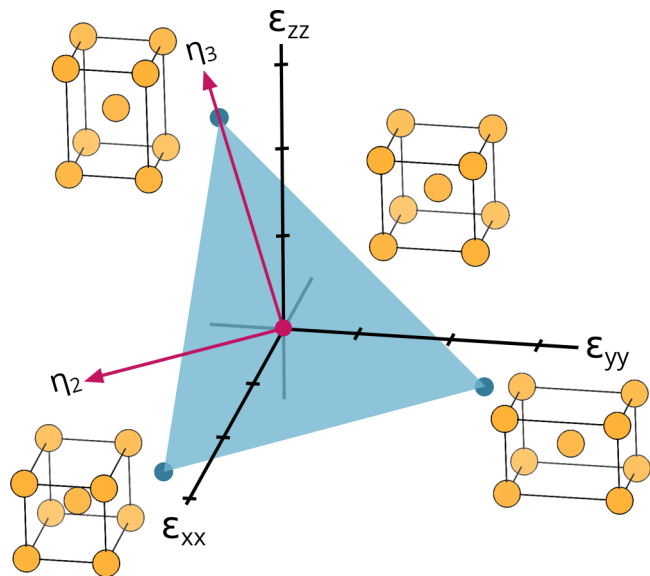


FIG. 1. An illustration of dimensionality reduction through OPs in the normal (Hencky) strain space of a bcc crystal (origin, pictured upper right). In this case, the three equivalent Bain pathways—tetragonal distortions to the three plotted points, which correspond to fcc lattices—lie in a plane that is fully spanned by  $\eta_2$  and  $\eta_3$ , which are defined by Eqs. (4) and (5). A representative structure is illustrated for each point.

$\eta_3$  will remain unchanged and is therefore referred to as an invariant subspace.

Completing the space of  $\sigma$ , the magnitude of the vector orthogonal to  $\eta_2$  and  $\eta_3$  can be represented as

$$\eta_1 = (\epsilon_{xx} + \epsilon_{yy} + \epsilon_{zz})/\sqrt{3}, \quad (6)$$

which measures symmetry-preserving volumetric dilation [23]; as the most basic type of deformation, it is typically denoted as  $\eta_1$ . The utility of these OPs is shown in Sec. IV A, which explores the  $\eta_2$ - $\eta_3$  surfaces of IrMn.

### B. A more complete method

The approach of the previous section can be generalized to parametrize many other crystal properties. To take one example, it is often of interest to describe long-range magnetic order that forms as a supercell of an underlying parent lattice. A given magnetic structure typically has several symmetrically equivalent variants, which give rise to coexisting magnetic domains. In the walls between domains, local moments spatially vary such that the ordering state gradually transitions from one variant to another. For a particular magnetic structure, well chosen OPs should concisely distinguish between all symmetrically equivalent variants and reasonably describe the domain-wall structures, as well as average to zero in the fully disordered (paramagnetic) state.

A periodic magnetic structure composed of  $n$  sites per unit cell is completely described in the  $3n$ -dimensional space  $\sigma$ , where

$$\sigma^T = (m_1^x, m_1^y, m_1^z, \dots, m_n^x, m_n^y, m_n^z). \quad (7)$$

We seek to redefine  $\sigma$  in terms of a new coordinate system with orthogonal basis vectors corresponding to useful OPs. As seen in the example of Sec. II A, the variants of a structure may lie in a lower-dimensional subspace of  $\sigma$ ; this is generally the case for order associated with a phase transition, including antiferromagnetism. Thus, to minimally describe sets of variants, OPs should be grouped into subspaces that are unchanged under the parent crystal's space group operations  $\{s_1, s_2, \dots, s_M\} \in \mathcal{S}$ ; while individual basis vectors may change, the space spanned by each invariant subspace must be constant under the application of any  $s$ . (Each fully decomposed invariant subspace corresponds to an irreducible representation of  $\mathcal{S}$ .)

It is in practice quite simple to identify such OPs. All symmetrically equivalent variants of a particular ordered state collectively span a subspace of  $\sigma$  that is described by projection  $P$ . As  $P$  is unchanged by the application of any  $s \in \mathcal{S}$ , its eigenvectors are grouped into invariant subspaces by eigenvalue [28] and provide a starting point for determining magnetic OPs. The remainder of the section elaborates on this procedure.

For any magnetic state,  $\mathbf{v}$ , in the  $3n$ -dimensional space of magnetic orderings  $\sigma$  [Eq. (7)], the application of the rotation, translation, and possible time inversion that compose every  $s \in \mathcal{S}$  can be represented as a  $3n \times 3n$  matrix,  $\mathbf{S}$ , that transforms  $\mathbf{v}$  as  $\mathbf{S}\mathbf{v}$ . As for the strain example, the variants of a magnetic structure can be related in this manner—the simplest example is spin-up and -down ferromagnetism, which are connected through time inversion. Often manually identifiable, the variants of some initial magnetic configuration  $\mathbf{v}_1$  (known from experiment or theory) can be rigorously generated as  $\mathbf{v}_k = \mathbf{S}\mathbf{v}_1$ . All  $\mathbf{S}$  applied to  $\mathbf{v}_1$  collectively generate  $K$  unique variants, which can be indexed arbitrarily as  $\mathbf{v}_k$ , with  $k = 1, \dots, K$ , where  $K$  is typically a fraction of the number of symmetry operations.

All  $\mathbf{v}_k$  collectively span a subspace described by the projection  $P$ , which can be represented as a  $3n \times 3n$  matrix

$$\mathbf{P} = \sum_{k=1}^K \mathbf{v}_k \cdot \mathbf{v}_k^\top. \quad (8)$$

$\mathbf{P}$  is invariant under the symmetry operations of the parent crystal. While individual elements in the sum are altered by the application of some  $\mathbf{S}$ , their total is not. There will always be  $K$  terms, and the application of symmetry can merely permute them per the rearrangement theorem [26]—otherwise, the magnetic structure would have additional symmetrically equivalent variants.

Each unique eigenvalue of  $\mathbf{P}$  represents an invariant subspace spanned by its associated eigenvectors. Given the invariance of  $\mathbf{P}$ , these subspaces are constant in any basis and minimally describe the considered variants. In our experience, common orthogonalization algorithms tend to yield surprisingly intuitive, high-symmetry eigenvalues for standard crystal structures. When this fails, a technique for rotating subspaces to maximally symmetrize their basis vectors is described in Appendix A of Ref. [23].

Scalar OPs  $\eta_i$  can be constructed from the high-symmetry eigenvectors,  $\mathbf{e}_i$ , of  $\mathbf{P}$  as simply

$$\eta_i = \mathbf{e}_i^\top \cdot \sigma. \quad (9)$$

The “primary” OPs, corresponding to nonzero eigenvalues, fully span  $\mathbf{P}$  and its constituent variants (if little else), whereas the remaining eigenvectors (with zero eigenvalues) orthogonalize unspanned space without physical motivation.

The projection can be extended to include the variants of additional ordered structures, possibly providing additional meaningful OPs. For example, in a cubic crystal, the six variants of FM order will be orthogonal to all AFM structures and form a distinct invariant subspace. The eigenvectors of this subspace yield OPs representing net magnetization in each direction, which are both intuitive and useful. When considering the variants of  $J$  unique structures, labeled as  $\mathbf{v}^j$ , the mathematical form of  $\mathbf{P}$  becomes

$$\mathbf{P} = \sum_{j=1}^J \sum_{k_j=1}^{K_j} \mathbf{v}_{k_j}^j \cdot \mathbf{v}_{k_j}^{j\top}, \quad (10)$$

where  $k_j$  indexes the  $K_j$  variants of  $\mathbf{v}^j$ . All structures must be described in the same initial space  $\sigma$ , requiring a common supercell commensurate with each ordering. A general procedure to identify such supercells is described in Ref. [25].

Within a single irreducible subspace, the variants of any configuration are equidistant from the origin, collectively lying on a hypersphere in the subspace. The radii of these hyperspheres typically vary among irreducible subspaces, ranging from zero in irreducible subspaces that are not required to distinguish between variants to some finite value in subspaces that capture the symmetry-breaking phase transformation. In general, hypersphere radii differ across symmetrically distinct irreducible subspaces. The eigendecomposition of  $\mathbf{P}$  naturally distinguishes among subspaces by providing the radii of the hyperspheres in a particular irreducible subspace (corresponding to the eigenvalues) and a set of spanning vectors (the eigenvectors with the same eigenvalue). In most material systems, such a decomposition will identify all unique irreducible subspaces, but this algorithm may fail if the hyperspheres formed by the variants have identical radii in multiple irreducible subspaces. Though such a scenario is extremely unlikely in real materials, it is easily solved by constructing order parameters following the algorithms outlined in Refs. [23–25].

Ultimately, OPs obtained in the above manner enable identification of direct pathways among variants and, in principle, magnetic domains. This task can often be simplified by noting how the energy scale of a moment's magnitude is generally larger than that of its orientation [15], motivating an initial assumption of constant local moment magnitudes. The application of magnetic OPs is demonstrated in Secs. IV B and IV C for IrMn and IrMn<sub>3</sub>, respectively.

### III. METHODS

In Sec. IV A, we explore the relationship between strain and magnetism for FM, AFM, and paramagnetic (PM) IrMn. PM structures were approximated using a 16-atom special quasirandom structure [29,30]. For each magnetic state,

collinearly spin-polarized DFT calculations (spin-orbit coupling is negligible at these energy scales) were performed for an evenly spaced triangular grid of 666  $\eta_2$  and  $\eta_3$  pairs, while volume (corresponding to  $\eta_1$ ) was allowed to relax. Simulations were performed using the Vienna *Ab initio* Simulation Package (VASP) [31,32], employing the generalized gradient approximation as parameterized by Perdew, Burke, and Ernzerhof [33] and projector-augmented wave potentials [34]. Calculations used a 520 eV plane-wave cutoff and a  $\Gamma$ -centered  $k$ -point mesh with a linear density of 33 Å.

In Secs. IV B and IV C, the method of Sec. II is applied to generate OPs describing the AFM structures of  $L1_0$  IrMn and  $L1_2$  IrMn<sub>3</sub>. These are used to study MAE and domain walls in both materials, requiring the consideration of noncollinear magnetism and spin-orbit coupling, which is considered scalar-relativistically in VASP. To map IrMn MAE, magnetic structures corresponding to 78 points in one quadrant of OP space were statically simulated. The same simulation parameters were used to compute the energy along pathways that connect symmetrically equivalent magnetic orderings in suitably defined order-parameter spaces. IrMn<sub>3</sub> was modeled using a  $10 \times 10 \times 10$  Monkhorst-Pack grid, as determined from the convergence of the  $d \rightarrow g$  energy barrier in Sec. IV C. Given the energy scales of these calculations, (relatively minor) magnetic dipolar corrections were applied according to the classical Hamiltonian [35]

$$H_{\text{dip}} = \frac{1}{2} \sum_{i,j} \frac{\mu_0}{4\pi r_{ij}^3} \left( \mathbf{m}_i \cdot \mathbf{m}_j - \frac{3}{r_{ij}^2} (\mathbf{m}_i \cdot \mathbf{r}_{ij})(\mathbf{m}_j \cdot \mathbf{r}_{ij}) \right), \quad (11)$$

where  $i$  and  $j$  index sites separated by  $\mathbf{r}_{ij}$  for up to third-nearest neighbors.

## IV. RESULTS

### A. Coupling of strain and magnetic order in IrMn

Figure 2 shows formation energy, volume, and average Mn moment as a function of the strain OPs  $\eta_2$  and  $\eta_3$  [Eqs. (4) and (5)] for AFM, PM, and FM IrMn. The center of each plot represents a B2 structure, i.e., a bcc lattice constructed from interlocking cubic sublattices of Ir and Mn. B2 is the simplest decoration of a bcc lattice and can be strained along the Bain path into three equivalent fcc variants, which are shown at the corners of each plot. Each fcc structure is associated with a variant of the experimentally realized  $L1_0$  ordering, which lie between fcc and bcc in the  $\eta_2$ - $\eta_3$  plane [36].

Regardless of the magnetic state, these  $L1_0$  structures form energetic minima, although the optimal degree of tetragonality ( $c/a$  ratio) varies significantly, as does the overall shape and scale of the energy landscape. The AFM  $L1_0$  variants are depicted in Fig. 3. Most striking is the AFM structure's  $-350$  meV/at formation energy, which is remarkably large for an intermetallic. This value is 192 meV/at lower than the minimum of the FM energy surface, indicating that a large portion of the structure's stability originates from AFM exchange interactions.

The importance of magnetism can also be seen in the energy difference among AFM fcc variants. AFM decoration of the bcc lattice breaks the symmetry of the Bain paths, resulting in fcc variants with fundamentally different magnetic states.

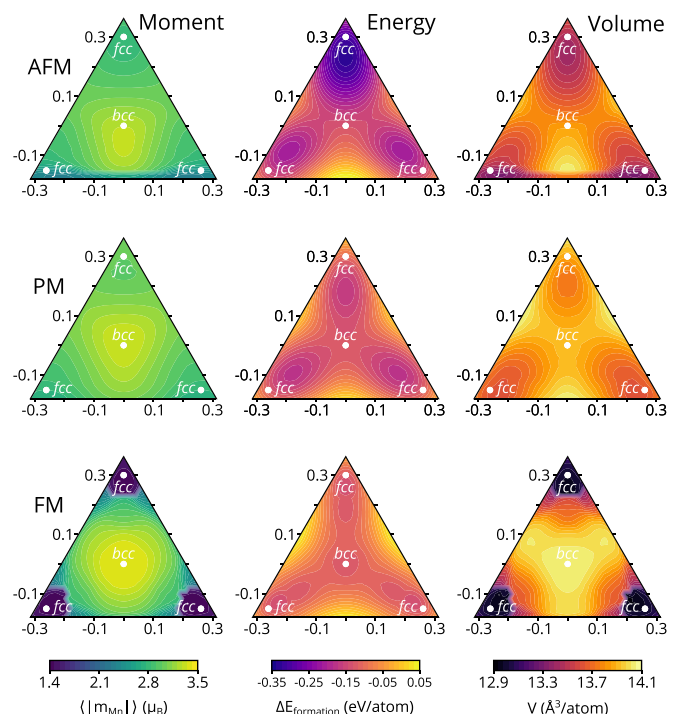


FIG. 2. Mn moment, formation energy, and relaxed volume calculated for three different magnetic orderings across  $\eta_2$ - $\eta_3$  strain space, which is defined by Eqs. (4) and (5) and illustrated as a plane in Fig. 1. The center of each plot corresponds to a high-symmetry, B2 (bcc) lattice. All minima are  $L1_0$  structures of varying tetragonality. The  $\eta_3$  axis is vertical and perpendicular to  $\eta_2$ ; the triangular boundary simply reflects the explored space.

In contrast, the PM (SQS) energy landscape in Fig. 2 displays threefold symmetry, which confirms its effective representation of magnetic disorder. For both AFM and PM orderings, volume correlates very closely with energy—the most compact configurations are also the most favored. These states also trend similarly in terms of moment magnitudes, which are maximized in the least efficiently packed (and high volume) bcc structure, although moment is not otherwise correlated to energy or volume. Indeed, the difference between the AFM and PM landscapes is largely the scale of energy and volume change, with the latter less extreme in both respects.

The FM plots, however, display an abrupt drop in volume and moment magnitude for lattices resembling fcc, corresponding to a subtle cusp in the energy landscape. Additionally, FM bcc IrMn is a local minimum while the absolute FM minimum is found around  $(\eta_2, \eta_3) = (0, 0.267)$  and its variants, closer to fcc ( $\eta_3 \approx 0.302$ ) than the optimal AFM  $L1_0$  structure ( $\eta_3 \approx 0.24$ ). Conversely, the most favorable PM structures lie midway between fcc and bcc lattices in the vicinity of  $(0, 0.15)$ , etc. The bcc-fcc energy difference also varies tremendously among magnetic states, ranging from approximately  $-130$  meV/at for AFM IrMn to  $-70$  meV/at for PM to a positive  $\sim 30$  meV/at in the FM case.

### B. IrMn magnetic structure

While the possibility of coupling magnetism and strain is intriguing, equiatomic IrMn clearly has an extremely sta-



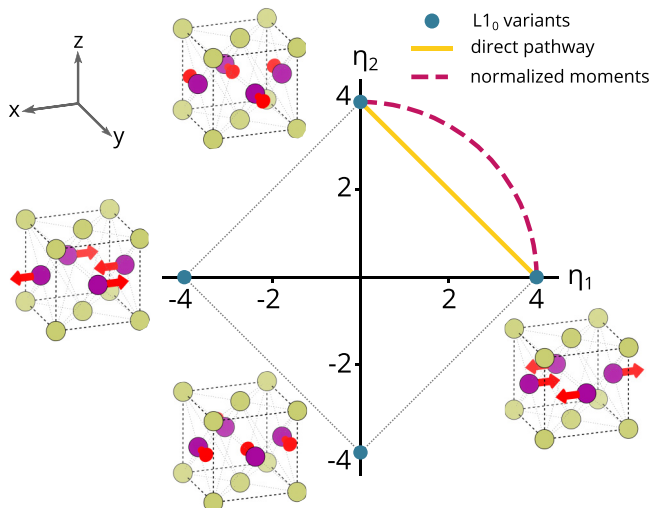


FIG. 3. The four symmetrically equivalent AFM variants of IrMn's  $L_{10}$  ground state plotted in OP-space alongside schematics. Mn atoms are represented by purple dots (dark); Ir are gold (light). The path between two variants in OP-space is shown, both directly (solid line) and with normalized atomic moment magnitudes (dashed line).

ble AFM  $L_{10}$  ground state. This structure provides a simple example for parametrizing magnetic order, with four checkerboard AFM variants, illustrated in Fig. 3, existing in the six-dimensional space defined by the components of the two Mn moments; Ir is effectively nonmagnetic and can be disregarded. This space can be divided into three two-dimensional invariant subspaces, only one of which is required to describe the considered variants. Following Sec. II, the primary OPs for AFM IrMn are

$$\eta_1 = (m_1^x - m_2^x)/\sqrt{2}, \quad (12)$$

$$\eta_2 = (m_1^y - m_2^y)/\sqrt{2}, \quad (13)$$

which form the axes of Fig. 3. The most direct path between neighboring variants is a Néel-type rotation of Mn moments—while somewhat trivial, this can be determined by interpolating in OP-space and normalizing moments, as shown by the dashed line in Fig. 3. Conservation of moment magnitude also suggests that the path between  $(\eta_1, \eta_2) = (4, 0)$  and  $(\eta_1, \eta_2) = (-4, 0)$  will pass through  $(0, \pm 4)$ .

Filling out the  $x$ - $y$  plane, two additional OPs form an invariant subspace describing in-plane FM ordering:

$$\eta_3 = (m_1^x + m_2^x)/\sqrt{2}, \quad (14)$$

$$\eta_4 = (m_1^y + m_2^y)/\sqrt{2}, \quad (15)$$

which are naturally orthogonal to the AFM subspace. Because the variants considered so far lie entirely in the  $x$ - $y$  plane,  $\eta_5$  and  $\eta_6$  will be unguided orthogonalizations of the  $z$ -dimension without further input. While it is generally accepted that the most favorable magnetic ordering of IrMn is indeed in-plane [15], the lowest energy path between two variants could in principle include out-of-plane components as in a Bloch-type domain wall.

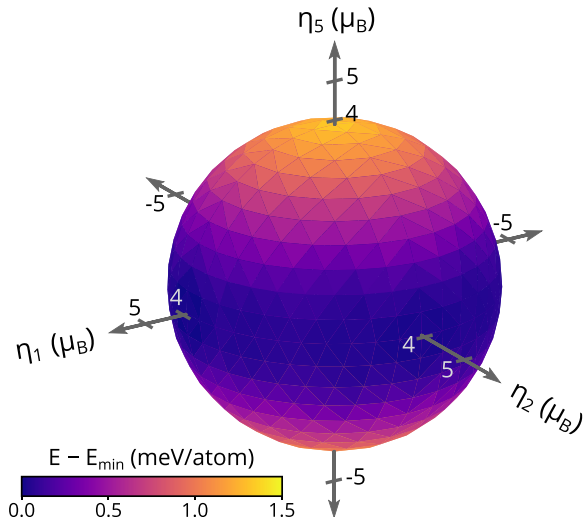


FIG. 4. The magnetic anisotropy energy of the IrMn configurations depicted in Fig. 3, with additional consideration of out-of-plane ( $z$ -aligned) orientations by inclusion of  $\eta_5$ . The sphere's equator corresponds to the constant-magnitude circumscription of the variants in Fig. 3 (dashed line).

Accounting for this possibility, the remaining space can be easily parametrized through the addition of otherwise identical [001]-aligned variants to a modified  $\mathbf{P}$  per Eq. (10). Its eigenvectors offer the additional primary OP,

$$\eta_5 = (m_1^z - m_2^z)/\sqrt{2}, \quad (16)$$

and its FM orthogonalization,

$$\eta_6 = (m_1^z + m_2^z)/\sqrt{2}. \quad (17)$$

Alongside  $\eta_1$  and  $\eta_2$ ,  $\eta_5$  enables exploration of the magnetic structure's full three-dimensional orientation space, which in this simple example is analogous to the alignment of  $\mathbf{m}_1^{\text{Mn}}$  (and  $-\mathbf{m}_2^{\text{Mn}}$ ) in the  $x$ ,  $y$ , and  $z$  directions for  $\eta_1$ ,  $\eta_2$ , and  $\eta_5$ , respectively. This space is explored using DFT (see Sec. III) in Fig. 4, which effectively depicts the structure's MAE. With minima near  $(\pm 2, 0, 0)$  and  $(0, \pm 2, 0)$ , this surface confirms the stability of the  $x$ - $y$  plane variants initially presented in Fig. 3 (as well as standard expressions of MAE [15]). While formal OPs are probably unnecessary to understand this simple structure, the parametrization of more complicated, noncollinear AFM orderings is less immediately obvious.

### C. IrMn<sub>3</sub> magnetic structure

The simple triangular AFM structure of  $L_{12}$  IrMn<sub>3</sub> has eight variants, which are depicted in Fig. 5. They collectively span a three-dimensional subspace of a nine-dimensional configuration space, which can be described by the primary OPs,

$$\eta_1 = (2m_1^x - m_2^x - m_3^x)/\sqrt{6}, \quad (18)$$

$$\eta_2 = (-m_1^y + 2m_2^y - m_3^y)/\sqrt{6}, \quad (19)$$

$$\eta_3 = (-m_1^z - m_2^z + 2m_3^z)/\sqrt{6}. \quad (20)$$

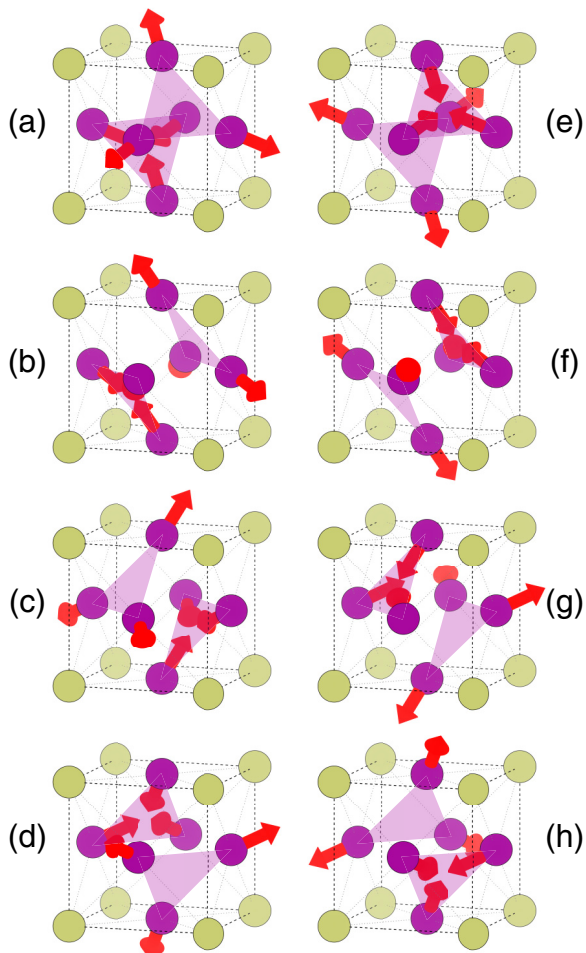


FIG. 5. The eight distinct but symmetrically equivalent variants of  $L_{12}$   $\text{IrMn}_3$ 's simple triangular magnetic ordering. The alphabetical labels correspond to points plotted in Fig. 6, and they are used to describe the pathways analyzed in Figs. 7 and 8.

Given  $\text{IrMn}_3$ 's cubic symmetry, inclusion of an FM variant in Eq. (10) introduces the additional OPs,

$$\eta_4 = (m_1^x + m_2^x + m_3^x)/\sqrt{3}, \quad (21)$$

$$\eta_5 = (m_1^y + m_2^y + m_3^y)/\sqrt{3}, \quad (22)$$

$$\eta_6 = (m_1^z + m_2^z + m_3^z)/\sqrt{3}. \quad (23)$$

The remaining space can be orthogonalized by  $\eta_7 = (m_2^x - m_3^x)/\sqrt{2}$ ,  $\eta_8 = (m_3^y - m_1^y)/\sqrt{2}$ , and  $\eta_9 = (m_1^z - m_2^z)/\sqrt{2}$ .

For a given variant,  $(\eta_1, \eta_2, \eta_3)$  is equivalent to the magnitude of Mn moment times the Miller index of the plane containing the (inward facing) moments, e.g., (111) for the variant depicted in Fig. 5(a). While not necessarily expected, this result is quite elegant. Altogether, the eight variants shown in Fig. 5 form a cube in the subspace of  $(\eta_1, \eta_2, \eta_3)$ , as plotted in Fig. 6.

This space enables a comparison of the moment rotations performed in Ref. [16] and the energy surface calculated by Ref. [19], both of which were considered measures of magnetic anisotropy. The four minima shown in Fig. 2 of Ref. [19] correspond to the variants  $a$ .,  $b$ .,  $d$ ., and  $g$ ., as illustrated in

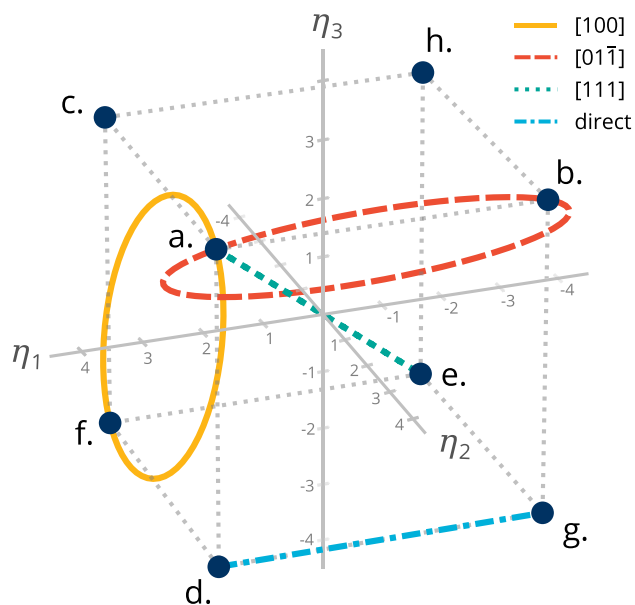


FIG. 6. Analogous to Fig. 3, the variants of  $\text{IrMn}_3$ 's  $L_{12}$  ground state plotted in three-dimensional OP-space. Paths corresponding to several variant-connecting rotations are drawn, as is a directly interpolated path. Variant labels refer to the structures illustrated in Fig. 5.

Fig. 5 and plotted in Fig. 6. Paths representing the [111] and  $[01\bar{1}]$  rotations of Ref. [16] (the latter  $[110]$  in their convention) are also drawn in Fig. 6, as is a  $[100]$  rotation connecting face-diagonal variants  $a$ . and  $f$ .. Reference [19] describes the lowest energy path between variants as a “bobbing motion,” but their 0.14 meV/at barrier appears equivalent to the  $\cos^{-1}(-\frac{1}{3}) \approx 109.47^\circ$  rotation around  $[01\bar{1}]$  reported by Ref. [16], which has a maximum energy of 0.16 meV/at.

More simply than either of the previously employed methods, pathways among adjacent variants can be determined by interpolating in OP-space and relaxing moments. The direct connection between variants  $d$ . and  $g$ . is drawn in Fig. 6 and explored in Fig. 7. While nonprimary OPs must activate to conserve moment magnitudes, the transition is primarily described by  $\eta_{1-3}$  even after relaxation of moments, demonstrating the utility of the approach. The only other nonzero OPs are  $\eta_8$  and  $\eta_9$ ; ferromagnetic OPs remain zero, indicating that no net moment arises in the transition. Spin-orbit coupling leads to a computed barrier of 0.12 meV/atom, which is comparable to, if slightly lower than, previous calculations [13,16].

Although not explicitly stated, the energy surface in Ref. [19] seems to suggest that a similarly low-energy path connects face-diagonal variants such as  $a$ . and  $f$ .—however, to the best of our knowledge, no such continuous transition is possible. While all four variants connect to a structure corresponding to an identical single-moment constraint, the approached configurations are fundamentally distinct, demonstrating the need to more completely parametrize an energy surface, e.g., through OPs. While direct interpolation from  $a$ . to  $f$ . in OP-space has an extremely high energy barrier, Fig. 6 indicates that a (100)-type rotation connects face-diagonal variants—as a rotation, its energy barrier should originate from spin-orbit interactions.

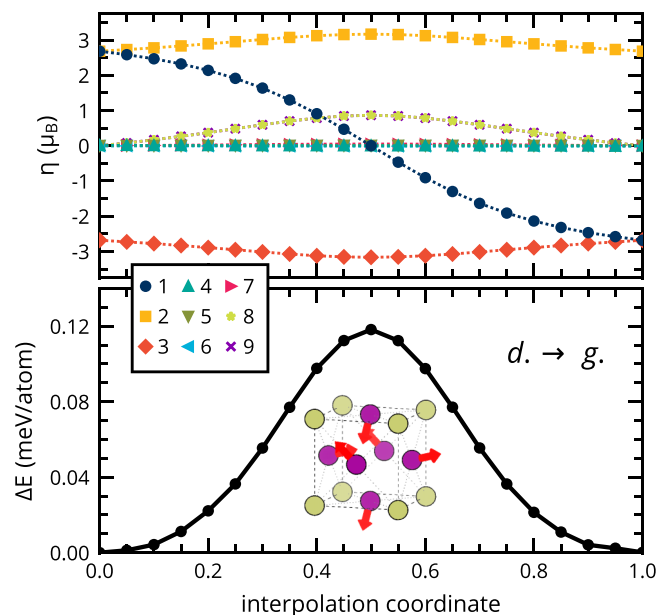


FIG. 7. The interpolated path from variant  $d.$  to  $g.$ , as drawn in Fig. 6. At 21 points, the local moment is relaxed using DFT, and the corresponding OPs and energy are above and below, respectively. A complete transition is equivalent to a rotation around  $[01\bar{1}]$  by  $\cos^{-1}(-\frac{1}{3}) \approx 109.47^\circ$ . The intermediate magnetic structure is also drawn in the lower panel.

This path is explored in Fig. 8. Not all intermediate structures are stable, so the directions of moments are constrained at each point. Interestingly,  $\eta_8$  and  $\eta_9$  remain the only nonzero, nonprimary OPs throughout the path, although their values are much larger than seen in Fig. 7. The rotation has a

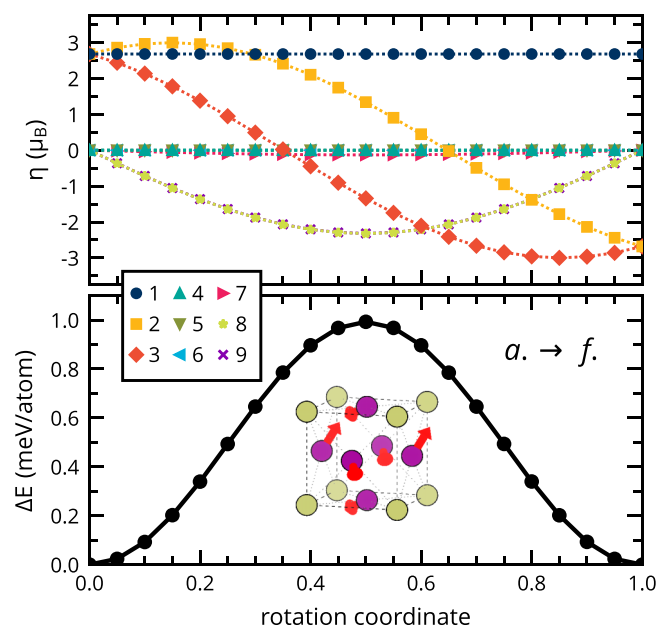


FIG. 8. The rotation of variant  $a.$  around  $[100]$ , in OP-space above with computed energy below. A  $180^\circ$  rotation (rotation coordinate 1) corresponds to variant  $f.$ , across the face of the cube formed in Fig. 6. An intermediate magnetic structure corresponding to a  $90^\circ$  rotation is also drawn in the lower panel.

1.0 meV/atom barrier, but given the possibility of transitioning through another corner variant (e.g.,  $a. \rightarrow c. \rightarrow f.$ ), it is unclear if the path will ever be realized in real domain walls. A similar question exists for (111) rotations connecting cube-diagonal (time-inverted) variants, which provide the “giant MAE” reported by Ref. [16].

## V. ADDITIONAL DISCUSSION

While the consideration of a midtransition structure as a periodic unit cell is fictitious—a physical domain wall consists of a continuous gradient of moment rotation—snapshots of OP-space can nonetheless approximate a pathway’s energy barrier, particularly for longer-range transitions where every locality deviates little from its neighbor. More completely, the free energy of a magnet with inhomogeneously varying magnetic OPs can be expressed as

$$F = \int_V \left[ f(T, \boldsymbol{\eta}(\mathbf{r})) + \sum_{i,j} \sum_{\alpha,\beta} K_{\alpha,\beta}^{i,j} \frac{\partial \eta_i}{\partial r_\alpha} \frac{\partial \eta_j}{\partial r_\beta} \right] d\mathbf{r}. \quad (24)$$

The homogeneous free energy  $f(T, \boldsymbol{\eta})$  is a function of temperature and local magnetic OPs  $\boldsymbol{\eta}(\mathbf{r})$ , which can serve as field variables tracking the spatial variation of local magnetic order as a function of position  $\mathbf{r}$ . (The homogeneous free energy  $f$  could also be made a function of strain [37].) The second integrand term accounts for energy penalties arising from gradients in magnetic OPs, which are determined by gradient energy coefficients  $K_{\alpha,\beta}^{i,j}$  that couple gradients in  $\eta_i$  and  $\eta_j$  along Cartesian directions  $\alpha$  and  $\beta$ .

Section II introduced a simple method to identify minimal magnetic OPs for arbitrary periodic magnetic orderings. We have also explored how the energy of two magnetic intermetallic compounds varies as a function of  $\boldsymbol{\eta}$ , which can provide a first-order estimate for domain-wall energy barriers—future work can determine the gradient energy coefficients  $K_{\alpha,\beta}^{i,j}$  by calculating excess energies for supercells containing spatial variations in magnetic OPs, which could be determined from Heisenberg exchange interactions. A first-principles-parametrized phenomenological free-energy description such as Eq. (24) will then not only enable a calculation of the excess free energies of magnetic domain walls, but also the minimal free-energy microstructure of multiple coexisting domains through a variational minimization of  $F$  with respect to  $\boldsymbol{\eta}(\mathbf{r})$ .

While the use of OPs does not inherently simplify the free-energy integrand of Eq. (24), we have shown how pathways connecting symmetrically equivalent variants can be largely described by primary OPs corresponding to a single subspace (see Fig. 7). Indeed, the nonzero secondary OPs serve primarily to conserve local moment magnitude and directly follow from primary OP values. The homogeneous free energy in Eq. (24), for example, can be expressed exclusively in terms of primary OPs by coarse graining out the secondary OPs using standard techniques from statistical mechanics [38], reducing the dimensionality of the free-energy model.

Although the investigation of strain serves primarily as an example, it suggests a possible connection, if not direct coupling, between a high-temperature  $\beta$ -IrMn phase and magnetic disordering at the Néel temperature. While IrMn adopts a nearly fcc  $L1_0$  structure at low temperatures, a bcc

B2 ordering at elevated temperature has been hypothesized on the basis of “metallographic observation of solidification deposits” [4]. Figure 2 illustrates how the  $\eta_2$ - $\eta_3$  energy surface of PM IrMn is much shallower than that of the AFM state, making it easier for anharmonic vibrational excitations to stabilize a B2 phase. Indeed, the PM energy landscape is similar to that of other compounds that undergo phonon-driven tetragonal-cubic phase transitions [36,39]. While the temperature (1223 K) of this transition is prohibitive to any practical application, further study could elucidate interesting physics and provide insight for identifying more accessible magnetically coupled phase transitions.

## VI. SUMMARY AND CONCLUSION

We have proposed a general method for parametrizing antiferromagnetic structures, applying the technique to study  $L1_0$  IrMn and  $L1_2$  IrMn<sub>3</sub>. In IrMn, we first characterized the interplay of crystalline (fcc, bcc, and the Bain paths that connect them) and magnetic (AFM, FM, PM) structure, noting the enormous energy reduction associated with its preferred AFM ordering and influence of magnetism on the strain dependence of energy.

The consideration of strain demonstrated a method for generating order parameters, which for magnetic structures can be summarized as follows:

(i) Identify the minimal unit cell describing magnetic structures of interest, which establishes the magnetic space of  $\sigma$  in Eq. (7).

(ii) Determine all variants  $v_k$  of an initial structure, typically through application of symmetry operation representations.

(iii) Calculate  $P = \sum_k v_k \cdot v_k^T$  per Eq. (8).

(iv) OPs correspond to eigenvectors of  $P$  by Eq. (9).

(v) If desired, expand  $P$  with additional magnetic orderings to expand the OP-space per Eq. (10), repeating the previous steps.

We used this framework to perform a first-principles study of the magnetic properties of IrMn and IrMn<sub>3</sub>, assessing their magnetic anisotropy and determining paths between symmetrically equivalent variants.

## ACKNOWLEDGMENTS

We thank J. C. Thomas for the code used in generating symmetry matrices. This work was supported by the National Science Foundation through the MRSEC Program Grant No. DMR-1720256 (IRG-1). Use was made of computational facilities purchased with funds from the National Science Foundation (CNS-1725797) and administered by the Center for Scientific Computing (CSC). The CSC is supported by the California NanoSystems Institute and the Materials Research Science and Engineering Center (MRSEC; NSF DMR 1720256) at UC Santa Barbara. F.W. was additionally supported by the Department of Defense through the National Defense Science & Engineering Graduate (NDSEG) Fellowship Program.

- 
- [1] J. Nogués and I. K. Schuller, *J. Magn. Magn. Mater.* **192**, 203 (1999).
- [2] V. Baltz, A. Manchon, M. Tsoi, T. Moriyama, T. Ono, and Y. Tserkovnyak, *Rev. Mod. Phys.* **90**, 015005 (2018).
- [3] T. Jungwirth, J. Sinova, A. Manchon, X. Marti, J. Wunderlich, and C. Felser, *Nat. Phys.* **14**, 200 (2018).
- [4] H. Okamoto, *J. Phase Equilib.* **17**, 60 (1996).
- [5] I. Tomeno, H. N. Fuke, H. Iwasaki, M. Sahashi, and Y. Tsunoda, *J. Appl. Phys.* **86**, 3853 (1999).
- [6] A. Sakuma, K. Fukamichi, K. Sasao, and R. Y. Umetsu, *Phys. Rev. B* **67**, 024420 (2003).
- [7] M. Ali, C. H. Marrows, M. Al-Jawad, B. J. Hickey, A. Misra, U. Nowak, and K. D. Usadel, *Phys. Rev. B* **68**, 214420 (2003).
- [8] A. Kohn, A. Kovács, R. Fan, G. J. McIntyre, R. C. C. Ward, and J. P. Goff, *Sci. Rep.* **3**, 2412 (2013).
- [9] J. M. Taylor, A. Markou, E. Lesne, P. K. Sivakumar, C. Luo, F. Radu, P. Werner, C. Felser, and S. S. P. Parkin, *Phys. Rev. B* **101**, 094404 (2020).
- [10] O. Gomonay, T. Jungwirth, and J. Sinova, *Phys. Rev. Lett.* **117**, 017202 (2016).
- [11] W. Zhang, W. Han, S.-H. Yang, Y. Sun, Y. Zhang, B. Yan, and S. S. P. Parkin, *Sci. Adv.* **2**, e1600759 (2016).
- [12] H. Chen, Q. Niu, and A. H. MacDonald, *Phys. Rev. Lett.* **112**, 017205 (2014).
- [13] S. Jenkins, R. W. Chantrell, and R. F. L. Evans, *Phys. Rev. Mater.* **5**, 034406 (2021).
- [14] R. Y. Umetsu, M. Miyakawa, K. Fukamichi, and A. Sakuma, *Phys. Rev. B* **69**, 104411 (2004).
- [15] R. Y. Umetsu, A. Sakuma, and K. Fukamichi, *Appl. Phys. Lett.* **89**, 052504 (2006).
- [16] L. Szunyogh, B. Lazarovits, L. Udvardi, J. Jackson, and U. Nowak, *Phys. Rev. B* **79**, 020403(R) (2009).
- [17] G. Vallejo-Fernandez, L. E. Fernandez-Outon, and K. O’Grady, *Appl. Phys. Lett.* **91**, 212503 (2007).
- [18] B. Craig, R. Lamberton, A. Johnston, U. Nowak, R. W. Chantrell, and K. O’Grady, *J. Appl. Phys.* **103**, 07C102 (2008).
- [19] S. Jenkins, R. W. Chantrell, T. J. Klemmer, and R. F. L. Evans, *Phys. Rev. B* **100**, 220405(R) (2019).
- [20] D. L. Mills, *Phys. Rev. B* **3**, 3887 (1971).
- [21] D. Grohol, K. Matan, J. H. Cho, S.-H. Lee, J. W. Lynn, D. G. Nocera, and Y. S. Lee, *Nat. Mater.* **4**, 323 (2005).
- [22] H. T. Stokes and D. M. Hatch, *Phase Trans.* **34**, 53 (1991).
- [23] J. C. Thomas and A. Van der Ven, *J. Mech. Phys. Solids* **107**, 76 (2017).
- [24] J. C. Thomas and A. Van der Ven, *Phys. Rev. B* **96**, 134121 (2017).
- [25] A. R. Natarajan, J. C. Thomas, B. Puchala, and A. Van der Ven, *Phys. Rev. B* **96**, 134204 (2017).
- [26] M. Tinkham, *Group Theory and Quantum Mechanics* (McGraw-Hill, New York, 1964).
- [27] A. Wills, *J. Phys. IV France* **11**, Pr9-133 (2001).
- [28] J. M. Ziman, *Elements of Advanced Quantum Theory* (Cambridge University Press, Cambridge, 1969).
- [29] A. Zunger, S.-H. Wei, L. G. Ferreira, and J. E. Bernard, *Phys. Rev. Lett.* **65**, 353 (1990).



- [30] I. Abrikosov, A. Ponomareva, P. Steneteg, S. Barannikova, and B. Alling, *Curr. Opin. Solid State Mater. Sci.* **20**, 85 (2016).
- [31] G. Kresse and J. Furthmüller, *Comput. Mater. Sci.* **6**, 15 (1996).
- [32] G. Kresse and J. Furthmüller, *Phys. Rev. B* **54**, 11169 (1996).
- [33] J. P. Perdew, K. Burke, and M. Ernzerhof, *Phys. Rev. Lett.* **77**, 3865 (1996).
- [34] G. Kresse and D. Joubert, *Phys. Rev. B* **59**, 1758 (1999).
- [35] S. Blundell, *Magnetism in Condensed Matter* (Oxford University Press, 2001).
- [36] J. G. Goiri and A. Van der Ven, *Phys. Rev. B* **94**, 094111 (2016).
- [37] A. Van der Ven, J. Thomas, B. Puchala, and A. Natarajan, *Annu. Rev. Mater. Res.* **48**, 27 (2018).
- [38] M. Kardar, *Statistical Physics of Fields* (Cambridge University Press, Cambridge, 2007).
- [39] J. C. Thomas and A. Van der Ven, *Phys. Rev. B* **88**, 214111 (2013).